Supplementary Information for

The Labrador Sea as a conduit of AMOC variability on multiple time scales

Jia-Jia Chen*, M. Susan Lozier

*Corresponding author. Email: jiajiachen@gatech.edu

This PDF file includes:

Figs. S1 to S8
Table S1
References (24-32)

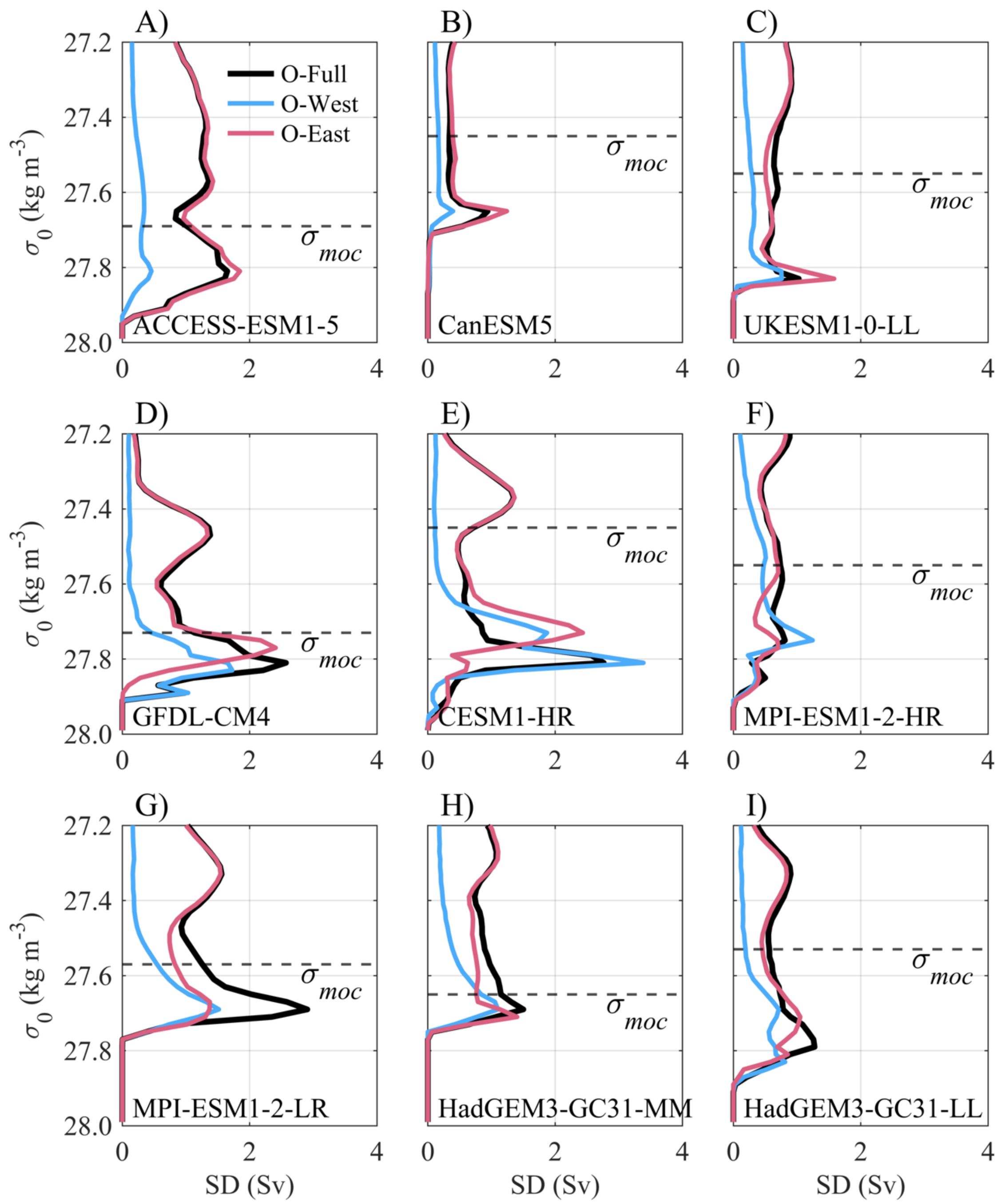

Fig. S1. Low-frequency (LF) variability of overturning stream function in density space derived from the suite of CMIP6 models used in this study. Similar to Fig. 1D of the main text but for the other nine models.

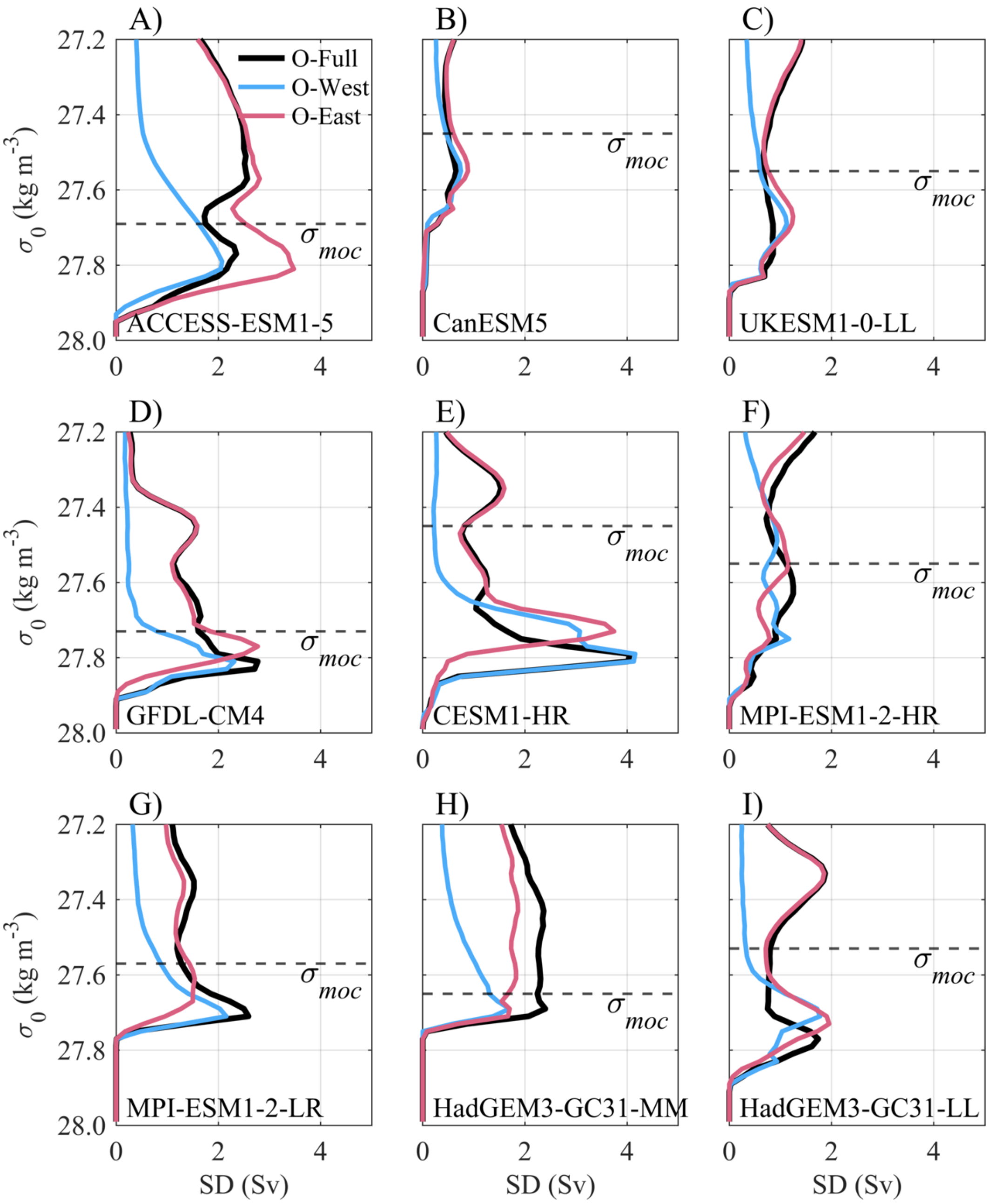

Fig. S2. High-frequency (HF) variability of overturning stream function in density space derived from the suite of CMIP6 models used in this study. Similar to Fig. 1f of the main text but for the nine models other than CESM2.

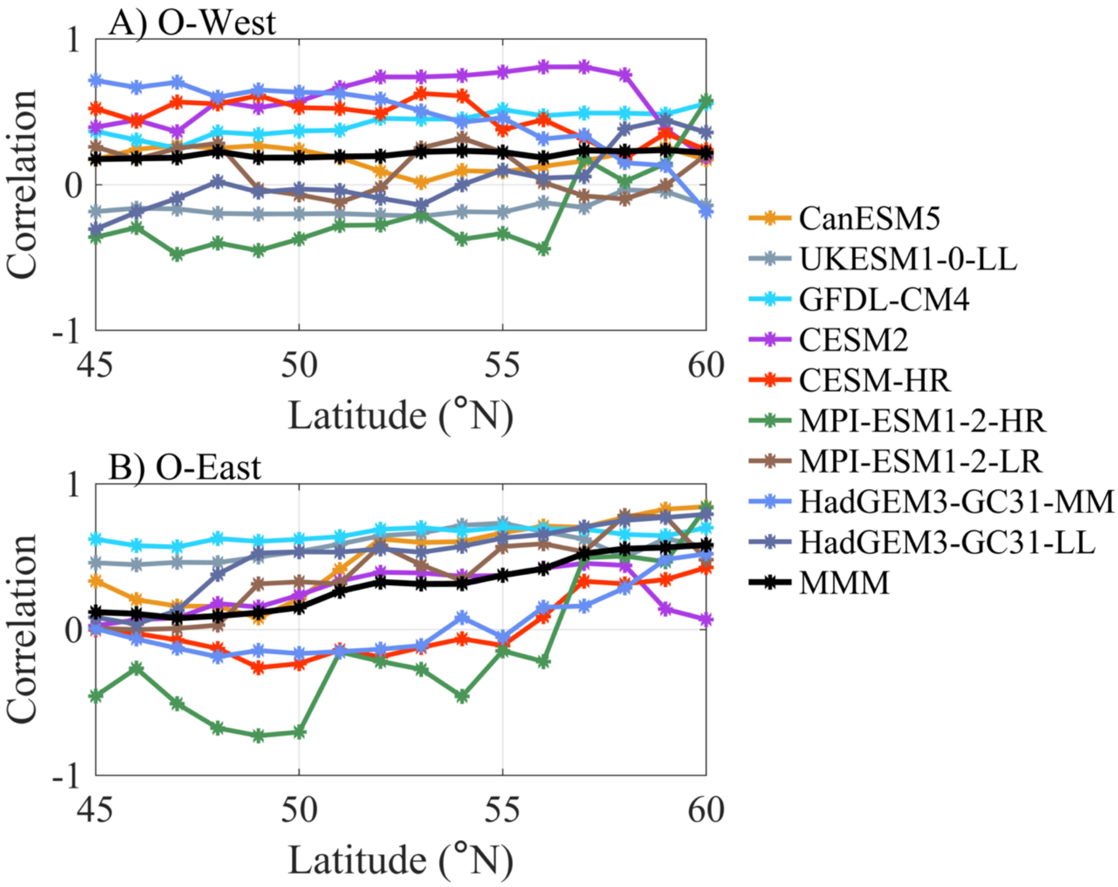

Fig. S3. Correlation of transport anomalies across different models. (A) Correlation coefficients between transport at σ_{SDmax} in O-West and MOC as a function of latitude (B) Correlation coefficients between transport at σ_{SDmax} in O-East and MOC as a function of latitude. All data have been processed with a 10-year low-pass filter.

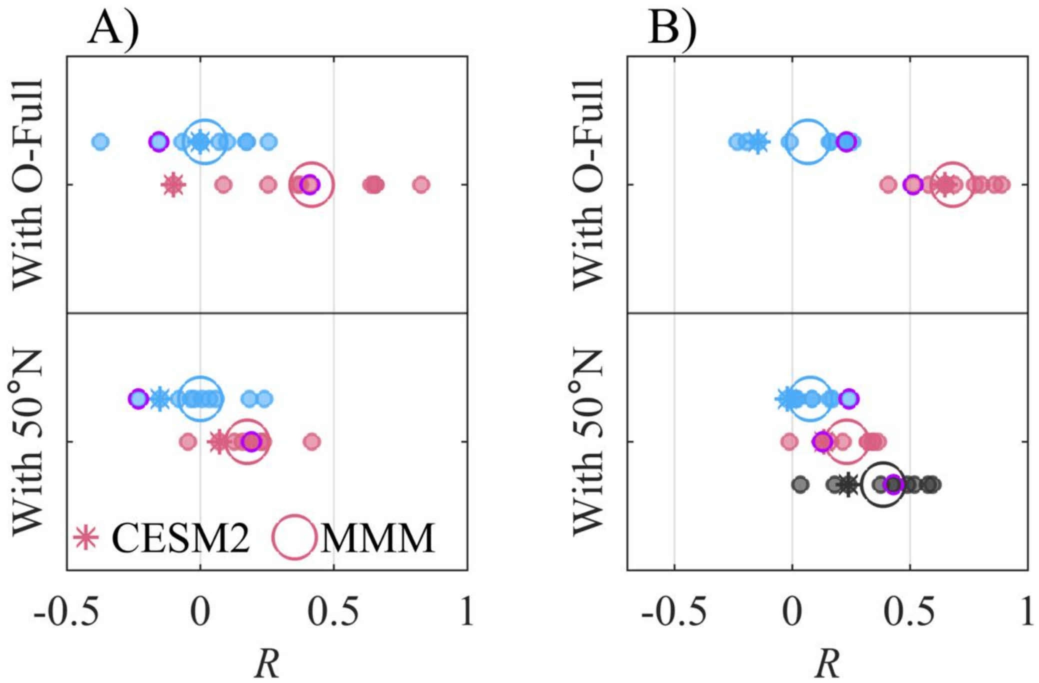

Fig. S4. Correlation of the transport at different densities with high-frequency MOC variability. (A) Correlation coefficients between the transport of O-West (blue) and O-East (pink) at σ_{SDmax} with the MOC at O-Full and MOC at 50°N. Small, filled circles denote all model results. The asterisk highlights the CESM2 correlation, and the purple outline highlights the correlation for the high-resolution model, CESM-HR. Large circles show the multi-model means. (B) Similar to (A) but for the correlation coefficients between the transport at σ_{moc} for O-West (blue) and O-East (pink) with MOC of O-Full and MOC at 50°N. Large black circle indicates the correlation between the MOCs at O-Full and 50°N. Similar to Fig. 2B and 2D of the main text but for HF variability.

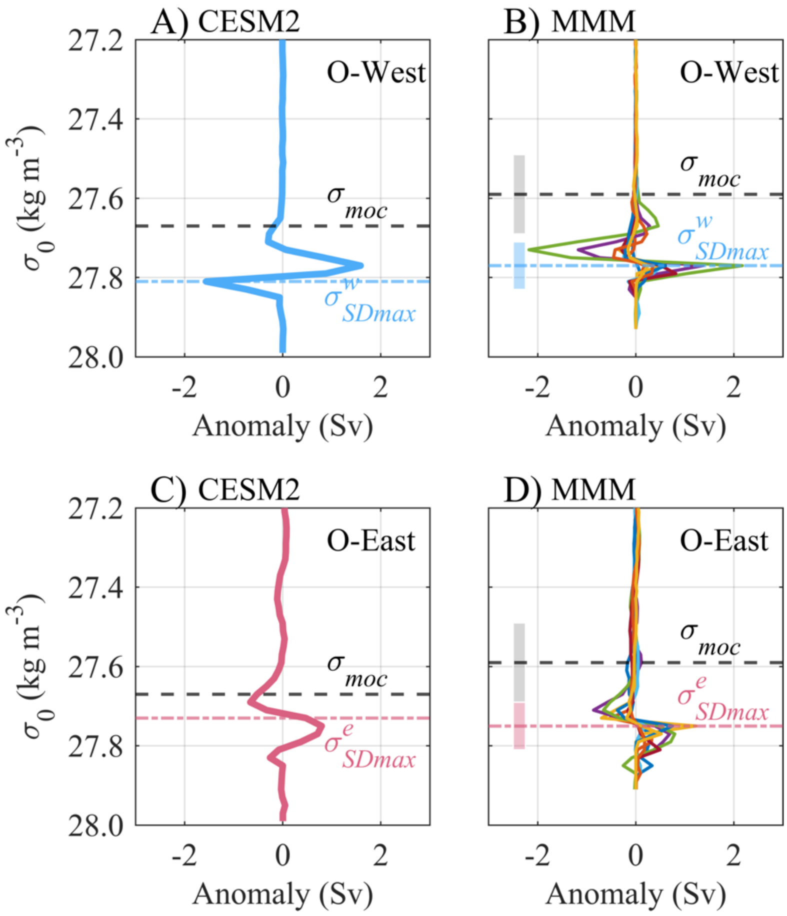

Fig. S5. Compensation pattern of low-frequency transport. (A) Composite of discrete transport anomalies constructed using transports at each density when there is a negative transport anomaly at σ^{w}_{SDmax}. Similar to Fig. 3A of main text but for negative anomalies at σ^{w}_{SDmax}. (B) As in (A), but for all models. Each model distribution is shifted in density space such that all σ^{w}_{SDmax} are aligned. The blue dashed line shows the mean σ^{w}_{SDmax}, and the black dashed line shows the mean σ_{moc} across all models, with the vertical bars depicting one standard deviation for corresponding densities. Similar to Fig. 3B of main text but for individual models. (C) Discrete transport anomaly of O-East, averaged over years with a positive transport anomaly at σ^{e}_{SDmax}. (D) Similar to (B) but for O-East.

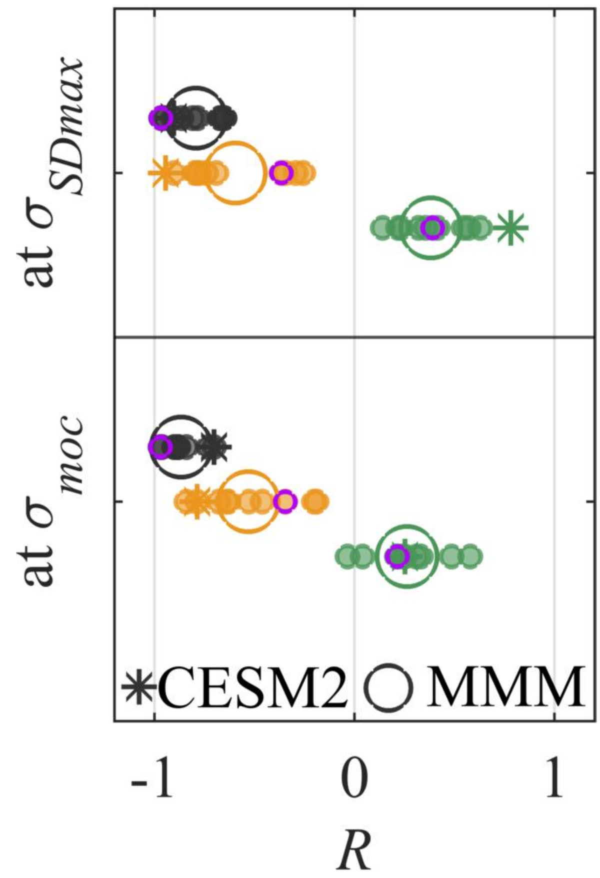

Fig. S6. Correlation between high-frequency outgoing and incoming transports across O-West. Correlation coefficients OW-Out and OW-In (black), OW-In and OE-Out (yellow), and OW-Out and OE-Out (green), using transports at σ_{SDmax} for the respective section. Small, filled circles denote all model results. The asterisk highlights the CESM2 correlation, and the purple outline highlights the correlation for the high-resolution model, CESM-HR. Large circles show the multi-model means. (bottom panel) Same as upper panel, but here correlations at σ_{moc} of O-Full are displayed. Similar to Fig. 4D of the main text but for HF variability.

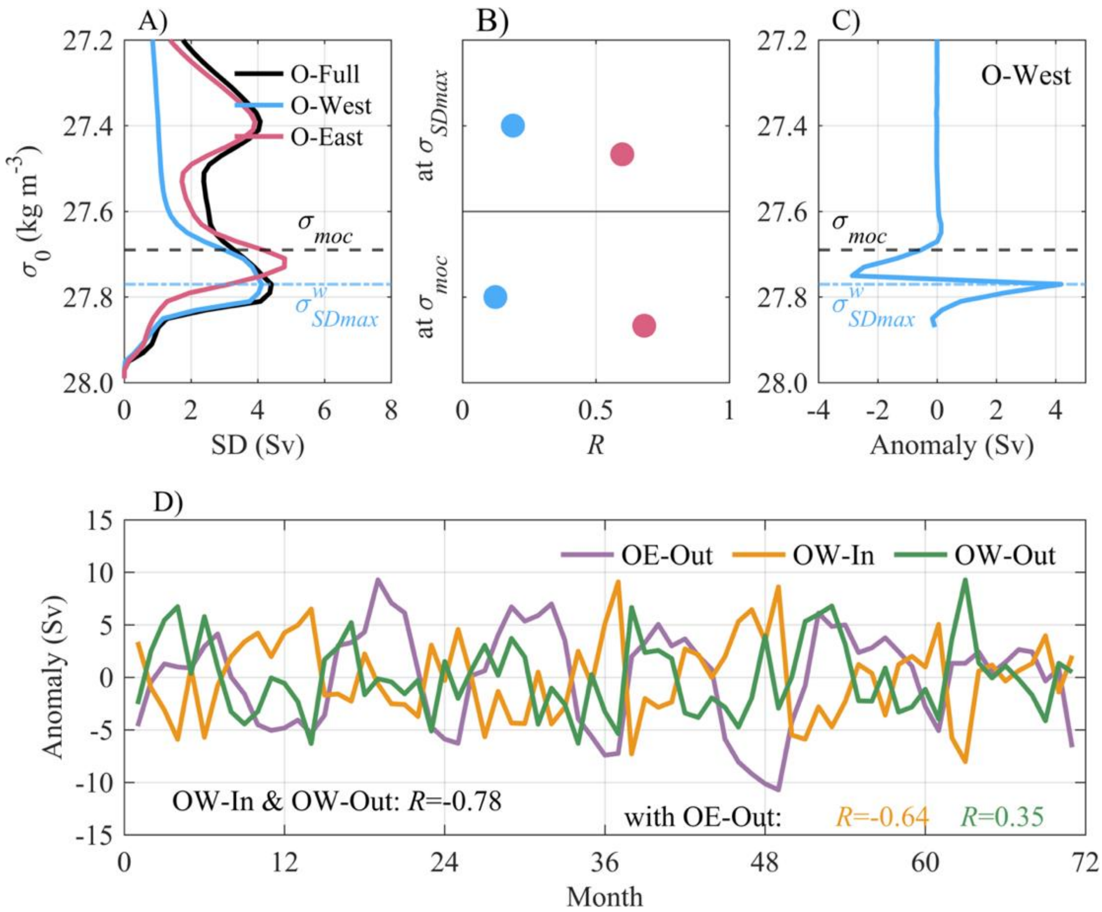

Fig. S7. Transport variability from the CESM2 simulations. (A) Monthly SD of transport across the OSNAP sections indicated. (B) Correlation coefficients between transports at O-West (blue) and O-East (pink) at their respective σ_{SDmax} with O-Full MOC (top panel), and the same, but with O-West and O-East transport calculated at σ_{moc} (bottom panel). (C) Discrete transport anomaly of O-West, averaged over months with a positive transport anomaly at σ^{w}_{SDmax}. (D) Time series of transport anomalies for southward flow of O-East (OE-Out), northward flow of O-West (OW-In), and southward flow of O-West (OW-Out) at the σ_{SDmax} for each component. Similar to Fig. 5 of the main text but for CESM2.

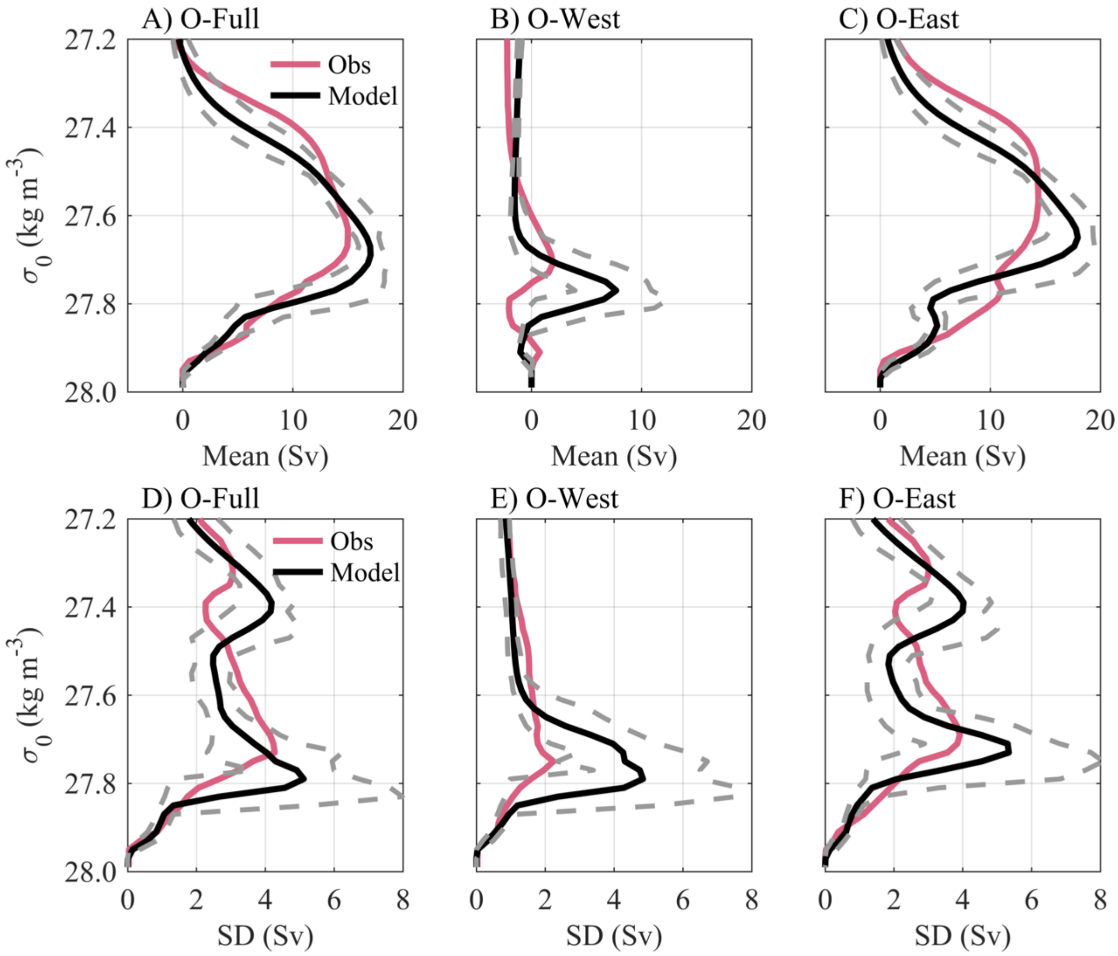

Fig. S8. Mean and variability of overturning stream function in density space. (A to C) Mean stream function across the three OSNAP sections from observations (red) and CESM simulations (black) as indicated. The model outputs were computed over all 71-month segments from the 300-year simulation. The gray dashed lines show the range of the simulated distribution. (D to F) As in (A to C) but for the monthly SD of the MOC stream function.

Table S1. Climate models used in this study. Most models are CMIP6 models, except CESM-HR, and were chosen because of their relatively small bottom density biases (*17*). Nominal horizontal resolution in °latitude × °longitude, vertical grid type and number of vertical levels and reference are displayed.

	Model name	Horizontal	Vertical	Ocean module
1	ACCESS-ESM1-5 (*24*)	1 × 1	z^* 50	MOM5
2	CanESM5 (*25*)	1 × 1	z 45	NEMO3.4.1
3	UKESM1-0-LL (*26*)	1 × 1	z^* 75	NEMO-HadGEM3-GO6.0
4	GFDL-CM4 (*27*)	0.25 × 0.25	$\rho - z^*$ 75	MOM6
5	CESM2 (*18*)	1 × 1	z 60	POP2
6	CESM-HR (*28*)	0.1 × 0.1	z 60	POP2
7	MPI-ESM1-2-HR (*29*)	0.4 × 0.4	z 40	MPIOM1.6.3
8	MPI-ESM1-2-LR (*30*)	1.5 × 1.5	z 40	MPIOM1.6.3
9	HadGEM3-GC31-MM (*31*)	0.25 × 0.25	z^* 75	NEMO-HadGEM3-GO6.0
10	HadGEM3-GC31-LL (*32*)	1 × 1	z^* 75	NEMO-HadGEM3-GO6.0

References

24. T. Ziehn, M. A. Chamberlain, R. M. Law, A. Lenton, R. W. Bodman, M. Dix, L. Stevens, Y.-P. Wang, J. Srbinovsky, The Australian Earth System Model: ACCESS-ESM1.5. *J. Southern Hemisphere Earth Syst. Sci.* **70**, 193–214 (2020).

25. N. C. Swart, J. Cole, V. Kharin, M. Lazare, J. Scinocca, N. Gillett, J. Anstey, V. Arora, J. Christian, S. Hanna, Y. Jiao, W. Lee, F. Majaess, O. Saenko, C. Seiler, C. Seinen, A. Shao, L. Solheim, K. von Salzen, D. Yang, B. Winter, The Canadian Earth System Model version 5 (CanESM5.0.3). *Geosci. Model Dev.* **5**, 1–68 (2019).

26. A. A. Sellar, C. G. Jones, J. P. Mulcahy, Y. Tang, A. Yool, A. Wiltshire, F. M. O'Connor, M. Stringer, R. Hill, J. Palmieri, S. Woodward, L. de Mora, T. Kuhlbrodt, S. T. Rumbold, D. I. Kelley, R. Ellis, C. E. Johnson, J. Walton, N. L. Abraham, M. B. Andrews, T. Andrews, A. T. Archibald, S. Berthou, E. Burke, E. Blockley, K. Carslaw, M. Dalvi, J. Edwards, G. A. Folberth, N. Gedney, P. T. Griffiths, A. B. Harper, M. A. Hendry, A. J. Hewitt, B. Johnson, A. Jones, C. D. Jones, J. Keeble, S. Liddicoat, O. Morgenstern, R. J. Parker, V. Predoi, E. Robertson, A. Siahaan, R. S. Smith, R. Swaminathan, M. T. Woodhouse, G. Zeng, M. Zerroukat, UKESM1: Description and Evaluation of the U.K. Earth System Model. *J. Adv. Model Earth Syst.* **11**, 4513–4558 (2019).

27. I. M. Held, H. Guo, A. Adcroft, J. P. Dunne, L. W. Horowitz, J. Krasting, E. Shevliakova, M. Winton, M. Zhao, M. Bushuk, A. T. Wittenberg, B. Wyman, B. Xiang, R. Zhang, W. Anderson, V. Balaji, L. Donner, K. Dunne, J. Durachta, P. P. G. Gauthier, P. Ginoux, J. C. Golaz, S. M. Griffies, R. Hallberg, L. Harris, M. Harrison, W. Hurlin, J. John, P. Lin, S. J. Lin, S. Malyshev, R. Menzel, P. C. D. Milly, Y. Ming, V. Naik, D. Paynter, F. Paulot, V. Rammaswamy, B. Reichl, T. Robinson, A. Rosati, C. Seman, L. G. Silvers, S. Underwood, N. Zadeh, Structure and Performance of GFDL's CM4.0 Climate Model. *J. Adv. Model Earth Syst.* **11**, 3691–3727 (2019).

28. S. Zhang, H. Fu, L. Wu, Y. Li, H. Wang, Y. Zeng, X. Duan, W. Wan, L. Wang, Y. Zhuang, H. Meng, K. Xu, P. Xu, L. Gan, Z. Liu, S. Wu, Y. Chen, H. Yu, S. Shi, L. Wang, S. Xu, W. Xue, W. Liu, Q. Guo, J. Zhang, G. Zhu, Y. Tu, J. Edwards, A. Baker, J. Yong, M. Yuan, Y. Yu, Q. Zhang, Z. Liu, M. Li, D. Jia, G. Yang, Z. Wei, J. Pan, P. Chang, G. Danabasoglu, S. Yeager, N. Rosenbloom, Y. Guo, Optimizing high-resolution Community Earth System Model on a heterogeneous many-core supercomputing platform. *Geosci. Model. Dev.* **13**, 4809–4829 (2020).

29. W. A. Müller, J. H. Jungclaus, T. Mauritsen, J. Baehr, M. Bittner, R. Budich, F. Bunzel, M. Esch, R. Ghosh, H. Haak, T. Ilyina, T. Kleine, L. Kornblueh, H. Li, K. Modali, D. Notz, H. Pohlmann, E. Roeckner, I. Stemmler, F. Tian, J. Marotzke, A Higher-resolution Version of the Max Planck Institute Earth System Model (MPI-ESM1.2-HR). *J. Adv. Model Earth Syst.* **10**, 1383–1413 (2018).

30. T. Mauritsen, J. Bader, T. Becker, J. Behrens, M. Bittner, R. Brokopf, V. Brovkin, M. Claussen, T. Crueger, M. Esch, I. Fast, S. Fiedler, D. Fläschner, V. Gayler, M. Giorgetta, D. S. Goll, H. Haak, S. Hagemann, C. Hedemann, C. Hohenegger, T. Ilyina, T. Jahns, D. Jimenéz-de-la-Cuesta, J. Jungclaus, T. Kleinen, S. Kloster, D. Kracher, S. Kinne, D. Kleberg, G. Lasslop, L. Kornblueh, J. Marotzke, D. Matei, K. Meraner, U. Mikolajewicz, K. Modali, B. Möbis, W. A. Müller, J. E. M. S. Nabel, C. C. W. Nam, D. Notz, S. S. Nyawira, H. Paulsen, K. Peters, R. Pincus, H. Pohlmann, J. Pongratz, M. Popp, T. J. Raddatz, S. Rast, R. Redler, C. H. Reick, T. Rohrschneider, V. Schemann, H. Schmidt, R. Schnur, U. Schulzweida, K. D. Six, L. Stein, I. Stemmler, B. Stevens, J. S. von Storch, F. Tian, A. Voigt, P. Vrese, K. H. Wieners, S. Wilkenskjeld, A. Winkler, E. Roeckner,

Developments in the MPI-M Earth System Model version 1.2 (MPI-ESM1.2) and Its Response to Increasing CO2. *J. Adv. Model Earth Syst.* **11**, 998–1038 (2019).

31. M. B. Menary, T. Kuhlbrodt, J. Ridley, M. B. Andrews, O. B. Dimdore-Miles, J. Deshayes, R. Eade, L. Gray, S. Ineson, J. Mignot, C. D. Roberts, J. Robson, R. A. Wood, P. Xavier, Preindustrial Control Simulations With HadGEM3-GC3.1 for CMIP6. *J. Adv. Model Earth Syst.* **10**, 3049–3075 (2018).

32. K. D. Williams, D. Copsey, E. W. Blockley, A. Bodas-Salcedo, D. Calvert, R. Comer, P. Davis, T. Graham, H. T. Hewitt, R. Hill, P. Hyder, S. Ineson, T. C. Johns, A. B. Keen, R. W. Lee, A. Megann, S. F. Milton, J. G. L. Rae, M. J. Roberts, A. A. Scaife, R. Schiemann, D. Storkey, L. Thorpe, I. G. Watterson, D. N. Walters, A. West, R. A. Wood, T. Woollings, P. K. Xavier, The Met Office Global Coupled Model 3.0 and 3.1 (GC3.0 and GC3.1) Configurations. *J. Adv. Model Earth Syst.* **10**, 357–380 (2018).